Nano Research Energy

ISSN 2791-0091 (print); 2790-8119 (online)
https://doi.org/10.26599/NRE.2026.9120238

Research Article

Strain-engineered interfacial water reorganization enables boosted HER/OER via intermediate adsorption modulation

Xiaojun Wang[1], Huilin Zhao[1], Xiaorui Zhang[1], Lei Li[2] (✉), Weiping Xiao[3], Qi Wu[4], Lei Wang[1] (✉), and Zexing Wu[1] (✉)

[1] *State Key Laboratory of Advanced Optical Polymer and Manufacturing Technology, Key Laboratory of Eco-chemical Engineering, Ministry of Education, International Science and Technology Cooperation Base of Eco-chemical Engineering and Green Manufacturing, College of Chemistry and Molecular Engineering, Qingdao University of Science & Technology, 53 Zhengzhou Road, Qingdao 266042, China*
[2] *College of Biological, Chemical Sciences and Engineering, Jiaxing University, Jiaxing 314001, China*
[3] *College of Science, Nanjing Forestry University, Nanjing 210037, China*
[4] *State Key Laboratory of New Textile Materials and Advanced Processing, Wuhan Textile University, Wuhan 430200, China*

Received: 9 April 2026 / **Revised:** 6 May 2026 / **Accepted:** 13 May 2026 / **Published date:** 18 June 2026

ABSTRACT

Developing cost-effective and high-performance bifunctional electrocatalysts is crucial for addressing the kinetic limitations of water electrolysis. Here, we successfully fabricate strained phosphorus-doped nickel-iron oxide on iron foam (P-$NiFe_2O_4$/IF) via simple corrosion-annealing coupling strategy. *In situ* Raman and electrochemical analyses reveal that the tensile lattice strain induced by P doping reorganizes the interfacial hydrogen-bond network and enhances its connectivity, accelerating proton transfer and deprotonation processes. Combined with theoretical calculations, it is confirmed that strain regulation effectively modulates the adsorption of *OH/*H, avoiding the *OH poisoning and poor deprotonation. In addition, the strain effect promotes surface reconstruction to generate active phases. Benefiting from the above advantages, P-$NiFe_2O_4$/IF exhibits excellent bifunctional electrocatalytic activity. A two-electrode electrolyzer constructed with P-$NiFe_2O_4$/IF requires only 1.45 V to reach 10 mA·cm^{-2} and maintains outstanding operational durability even under high current conditions. This research sheds light on fabricating efficient and robust bifunctional electrocatalysts for water-splitting by regulating interfacial water and intermediate adsorption via strain engineering.

KEYWORDS

strain engineering, hydrogen bond network, intermediate adsorption, bifunctional electrocatalysts

1 Introduction

Hydrogen energy, as clean, efficient and adaptable energy carrier, plays pivotal roles in the shift toward sustainable global energy landscape [1]. Among conventional hydrogen production technologies, water electrolysis has attracted increasing attentions due to its intrinsic environmental friendliness and strong scalability [2]. However, both the cathodic hydrogen evolution reaction (HER) and the anodic oxygen evolution reaction (OER) are thermodynamically uphill and kinetically sluggish, necessitating overpotentials far above the theoretical values [3]. Moreover, both half-reactions still depend on noble-metal electrocatalysts, which further hinders the advancement of water electrolysis [4]. Notably, nickel-iron (NiFe) based materials, characterized by earth abundance, numerous accessible active sites, and tunable coordination environments, are widely regarded as among the most promising non-precious metal catalysts for overcoming these issues [5]. However, challenges such as intrinsic activity, mismatched intermediate adsorption, and suboptimal mass transport hinder their industrial adoption [6, 7]. From the fundamental perspective, these bottlenecks can be attributed to the limited interfacial proton-transfer efficiency and the inadequate regulation of intermediate adsorption energies, thereby providing clear guidance for further catalyst optimization.

Both HER and OER involve proton-coupled electron transfer (PCET) processes [8]. Enhancing proton transport efficiency and accelerating deprotonation are thus critical for improving the catalytic performances of HER and OER [9, 10]. During the alkaline water electrolysis process, protons primarily migrate via the Grotthuss mechanism, moving in a relay process along hydrogen-bond networks [11]. Discontinuous or weakly bonded hydrogen-bond networks impede proton migration and thus reduce the efficiency of reaction kinetics [12]. Importantly, the hydroxyl binding energy (OHBE) directly regulates the interfacial water orientation and the hydrogen-bond network (HBN) configuration, while an optimal OHBE enhances network connectivity, thereby facilitating proton hopping [13, 14]. Since *OH adsorption strength is closely correlated with the OHBE, variations in OHBE not only regulate the interfacial HBN

© The Author(s) 2026. Published by Tsinghua University Press. The articles published in this open access journal are distributed under the terms of the Creative Commons Attribution 4.0 International License (http://creativecommons.org/licenses/by/4.0/), which permits use, distribution and reproduction in any medium, provided the original work is properly cited.

Address correspondence to Zexing Wu, splswzx@qust.edu.cn; Lei Wang, inorchemwl@126.com; Lei Li, leili@mail.zjxu.edu.cn

structure but also influence the energy requirements of individual reaction steps and their kinetic behaviors of both HER and OER [15]. Specifically, excessively strong *OH adsorption (high OHBE) blocks active sites, reduces the availability of hydrogen adsorption sites and increases the subsequent *OH → *O/*OOH transformation energy barriers. This decreases the coverage of active hydrogen and hinders the *OH deprotonation step [16, 17]. In contrast, overly weak adsorption (low OHBE) significantly increases the energy barrier for water dissociation [17], ultimately hindering the overall HER/OER kinetics. Thus, the synchronous optimization of intermediate adsorption behavior and hydrogen-bond network structure directly enhances electrocatalytic performance.

To achieve synchronous optimization, lattice strain engineering has recently emerged as effective means for boosting electrocatalytic performance, by adjusting the adsorption behavior of reaction intermediates [18]. Strain-induced modulation of the d-band center governs the adsorption-desorption dynamics of reaction intermediates [19]. Moreover, lattice strain substantially reshapes the catalyst-electrolyte interfacial environment, with consequent modulation of the overall catalytic reaction kinetics [20]. Heteroatom doping stands out among various strain-induction approaches owing to its ability to create precise, localized structural distortions and atomic-scale lattice deformations [21]. Benefiting from high valence electron density, phosphorus (P) effectively tunes catalyst electronic structures and lattice environments, leading to its widespread application [22]. However, elucidating the precise mechanisms by which P-induced lattice distortion controls intermediate adsorption, interfacial structure, and reaction kinetics remains significant challenge.

Herein, P doped transition metal oxide electrocatalyst (P-$NiFe_2O_4$/IF) was synthesized on iron foam (IF) through corrosion-annealing strategy, where P doping induces lattice strain, constructs seaurchin-like superhydrophilic architecture, and establishes three-dimensional hierarchical framework that facilitates mass transport. Electrochemical measurements demonstrate the superior catalytic performance of strain-engineered P-$NiFe_2O_4$/IF, requiring merely 340 mV to obtain 1 A·cm^{-2} for OER and 22 mV to reach 10 mA·cm^{-2} for HER in 1 M KOH. Through experimental and theoretical analyses, we elucidate the synergistic optimization mechanism for HER/OER: (1) The lattice strain induced by P doping reorganizes the interfacial water environment, accelerating water dissociation, proton transfer, and deprotonation processes. (2) The strain effect modulates the *H adsorption-desorption behavior, enabling more efficient HER via the Volmer-Heyrovsky pathway; Meanwhile, the combination of optimized *OH adsorption and lowered Ni-OOH formation energy barrier, ensures smooth OER process following the adsorption evolution mechanism (AEM). Therefore, P-$NiFe_2O_4$/IF delivers exceptional activity and long-term stability for industrial water splitting. This study offers important guidance for the rational construction and synergistic tuning of high-performance bifunctional electrocatalysts.

2 Experimental section

2.1 Synthesis of $NiFe_2O_4$/IF

The $NiFe_2O_4$/IF catalyst was prepared by simple corrosion and annealing strategy. Firstly, 2.0 mmol $NiCl_2·6H_2O$ was dissolved in 30 mL of deionized water under stirring. Then, the pretreated IF (two pieces, 1 cm × 1.5 cm) were placed in the solution and stirred at room temperature for 12 h. The product was rinsed with deionized water for 3 times and dried in vacuum at 60 °C for 6 h to obtain the precatalyst. Subsequently, the precatalyst was calcined in air at 400 °C for 2 h to yield the $NiFe_2O_4$/IF.

2.2 Synthesis of P-$NiFe_2O_4$/IF

The prepared $NiFe_2O_4$/IF was placed in a porcelain boat, the other porcelain boat containing 1.5 g of $NaH_2PO_2·H_2O$ positioned upstream in the tube furnace. The sample was heated to 350 °C with 5 °C·min^{-1} under H_2/Ar for two hours. The obtained sample is named as P-$NiFe_2O_4$/IF.

3 Results and discussion

3.1 Physical characterization

P-$NiFe_2O_4$/IF was constructed via a sequential process of room-temperature corrosion, thermal annealing, and low-temperature phosphorization (Fig. 1(a)). Scanning electron microscopy (SEM) images of P-$NiFe_2O_4$/IF (Figs. 1(b) and 1(c)) reveal characteristic seaurchin-like architecture, providing a more open structure with abundant accessible catalytic sites and favorable channels for mass transport [23]. Meanwhile, the superhydrophilic surface (contact angle = 0°, Fig. 1(d)) significantly promotes bulk mass transport and simultaneously favors the formation of continuous hydrogen-bond network [24, 25]. The X-ray diffraction (XRD) pattern of the P-$NiFe_2O_4$/IF shows characteristic reflections at 2θ = 30.3°, 35.7°, and 63.0°, matching with the (220), (311), and (440) facets of spinel $NiFe_2O_4$ (PDF#54-0964) [26]. The slight shift of these peaks to lower angles compared with pristine $NiFe_2O_4$/IF confirms that P doping induces lattice tensile strain (Fig. 1(e)) [27]. In the high-resolution transmission electron microscopy (HRTEM) images of P-$NiFe_2O_4$, lattice fringes with d-spacings of 0.26 and 0.16 nm can be clearly identified, which are attributed to the (311) and (440) planes of $NiFe_2O_4$ (Figs. 1(f)–1(h)) [28]. In comparison with the undoped sample (Figs. 1(i)–1(k)), P-$NiFe_2O_4$/IF displays slightly enlarged lattice fringes, supporting the lattice expansion detected in the XRD analysis. The above strain effect is further corroborated by geometric phase analysis (GPA, Fig. S1(a) in the Electronic Supplementary Material (ESM)). As revealed by element mapping (EDS) analysis, Fe, O, P, and Ni elements are uniformly dispersed within the P-$NiFe_2O_4$/IF sample (Fig. 1(l)).

X-ray photoelectron spectroscopy (XPS) was employed to comprehensively analyze the surface elemental distribution and elucidate the elemental valence states of the synthesized samples. As depicted in Fig. 2(a), the XPS survey spectra verify successful P incorporation. The Fe 2p XPS spectra of P-$NiFe_2O_4$/IF (Fig. 2(b)) are decomposed into four characteristic components: Fe^{2+} (709.3 eV, 722.7 eV), Fe^{3+} (712.0 eV, 725.6 eV), Fe-P (706.9 eV, 719.8 eV) and satellite peaks [22, 29]. Notably, the strained P-$NiFe_2O_4$/IF exhibits significant negative shift in the Fe 2p binding energy compared with unstrained $NiFe_2O_4$/IF. Two intense peaks observed at 129.4 and 130.3 eV in the P 2p spectrum (Fig. 2(c)) are attributed to the P $2p_{3/2}$ and P $2p_{1/2}$ orbitals, respectively [30]. The additional broad peak centered at 133.6 eV is attributed to surface-oxidized phosphorus species formed upon air exposure [31, 32], which is further supported by the characteristic P-O bonding signal observed in Fig. 2(d). The O 1s spectra (Fig. 2(d)) exhibits characteristic peaks corresponding to metal-oxygen bonds (M-O) and oxygen vacancies (O_V) [33]. Furthermore, the Ni 2p peak shifts toward lower binding energy after the introduction of lattice strain. However, the corresponding

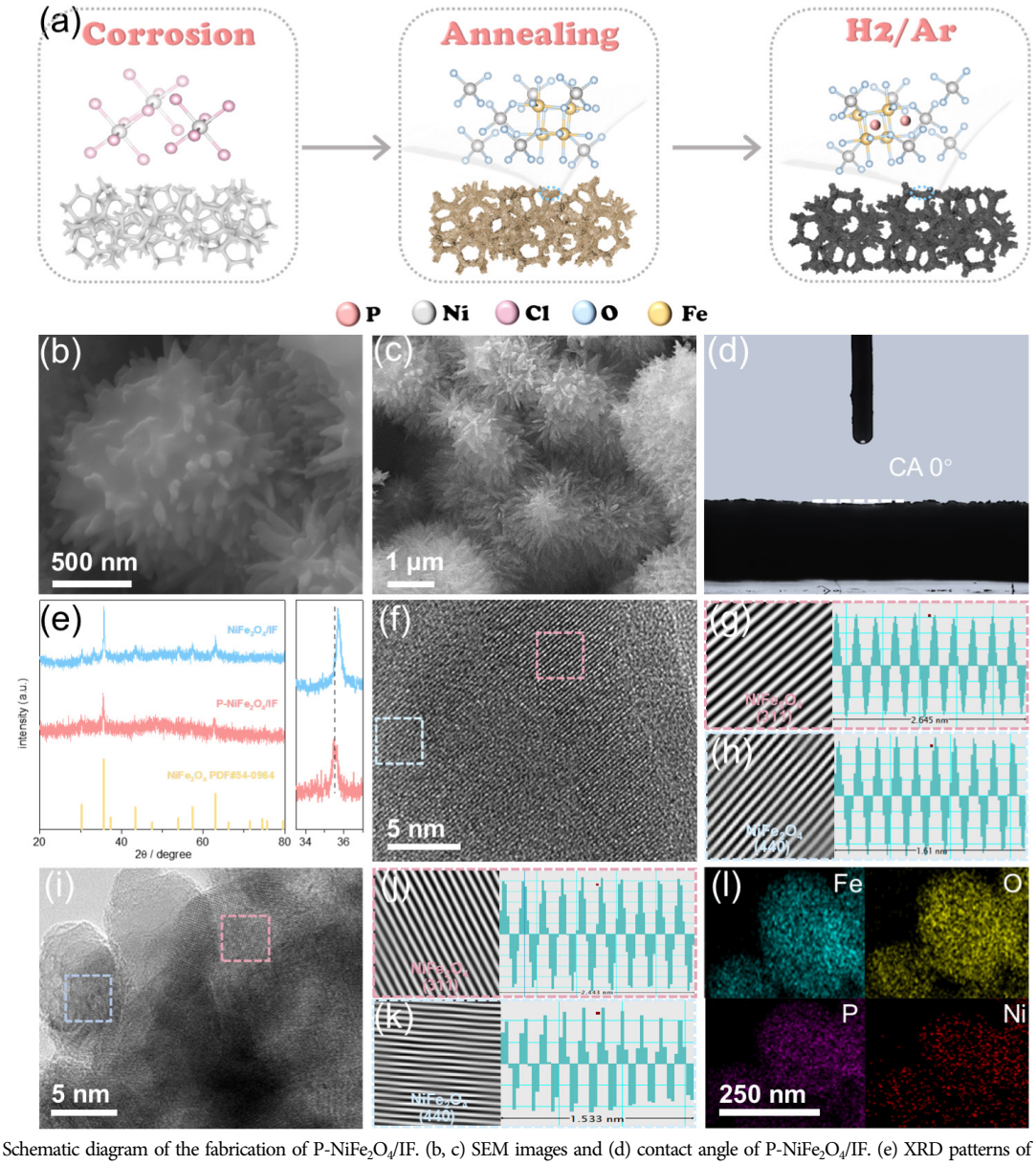


Figure 1 (a) Schematic diagram of the fabrication of P-$NiFe_2O_4$/IF. (b, c) SEM images and (d) contact angle of P-$NiFe_2O_4$/IF. (e) XRD patterns of the synthesized catalysts. HRTEM images of (f-h) P-$NiFe_2O_4$/IF and (i-k) $NiFe_2O_4$/IF. (l) EDS mapping images of P-$NiFe_2O_4$/IF.

XPS signal exhibits weak intensity owing to the relatively low surface Ni content (Fig. 2(e)). Thus, strain effect successfully modulates the metal valence state and creates favorable electronic environment for intermediate adsorption [34]. Ultraviolet photoelectron spectroscopy (UPS) analysis indicates that the strain generated by P doping reduces the catalyst W_f, facilitating interfacial charge transfer and accelerating catalytic reaction kinetics (Fig. 2(f)) [35].

3.2 Electrocatalytic performance of catalysts

A typical three-electrode system was employed to systematically evaluate the electrocatalytic performance of the prepared catalysts in 1 M KOH. Remarkably, the synthesis strategy and experimental conditions play crucial roles in determining the overall catalytic performance (Figs. S1(b)-S1(f) in the ESM). To distinguish the contribution of the reduction effect induced by the H_2/Ar atmosphere from that of P doping, comparative studies were conducted on $NiFe_2O_4$/IF before and after annealing in H_2/Ar atmosphere. The annealed sample is denoted as $NiFe_2O_4$/IF (H_2/Ar). XPS O 1s peak deconvolution indicates that $NiFe_2O_4$/IF (H_2/Ar) exhibits slight increase in O_V content compared with $NiFe_2O_4$/IF (Fig. S2(a) in the ESM, 36.23% vs. 34.65%), suggesting that the reductive nature of H_2 only moderately increases the O_V concentration in the catalyst. Nevertheless, XRD analysis of $NiFe_2O_4$/IF (H_2/Ar) reveals no obvious peak shift relative to $NiFe_2O_4$/IF (Fig. S2(b) in the ESM), indicating that H_2 reduction does not induce significant lattice strain. In contrast, P doping induces pronounced lattice strain (Figs. 1(e)-1(k) and Fig. S1(a) in the ESM). Furthermore, electrochemical measurements demonstrate that the performance enhancement resulting H_2 reduction is far inferior to that achieved by P doping (Figs. S2(c) and S2(d) in the ESM). Overall, the lattice strain is primarily induced by P doping and serves as the main contributor to the performance enhancement. In Fig. 3(a) and Figs. S2(e) and S2(f) in the ESM, P-$NiFe_2O_4$/IF exhibits outstanding HER activity, necessitating overpotentials of merely 22/155/218 mV to attain 10/100/500 mA·cm^{-2} (η_{10}, η_{100}, and η_{500}) in 1 M KOH, lower than $NiFe_2O_4$/IF (η_{10} = 28 mV, η_{100} = 281 mV, and η_{500} = 301 mV) and

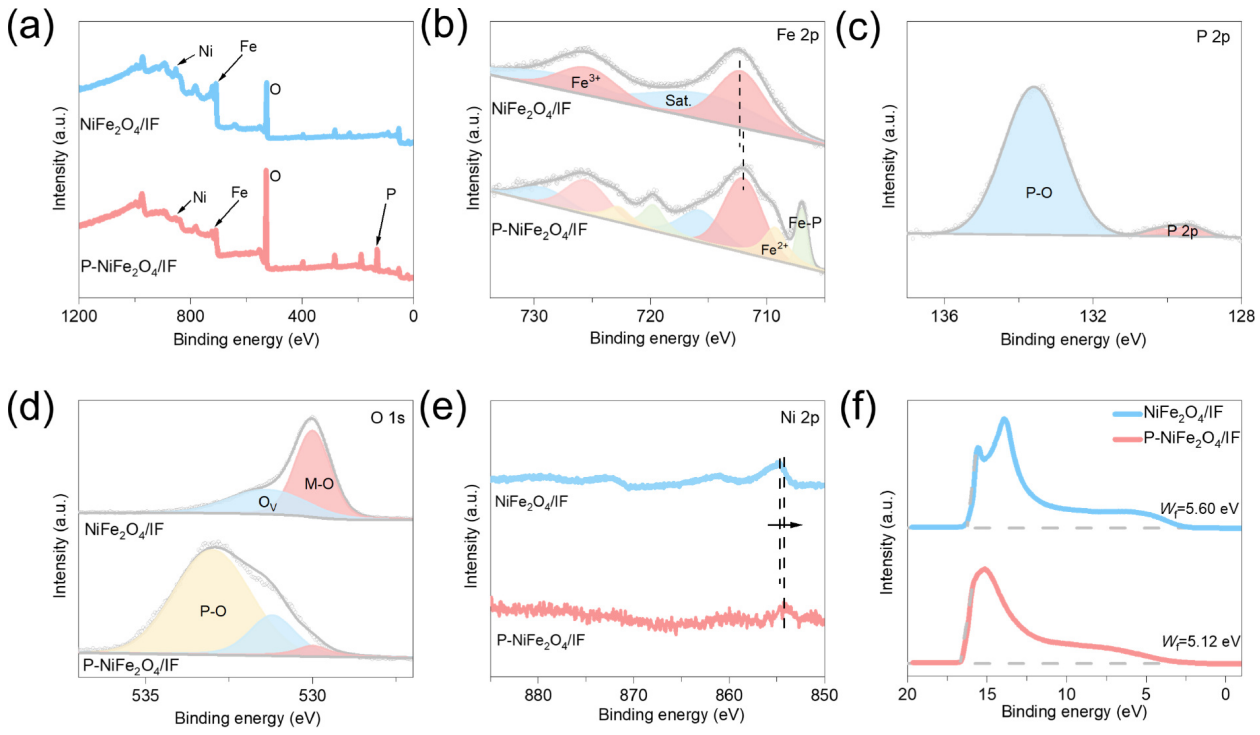


Figure 2 (a) XPS survey spectra. High-resolution XPS spectra of (b) Fe 2p, (c) P 2p, (d) O 1s and (e) Ni 2p of the synthesized catalysts. (f) UPS spectra of the synthesized catalysts.

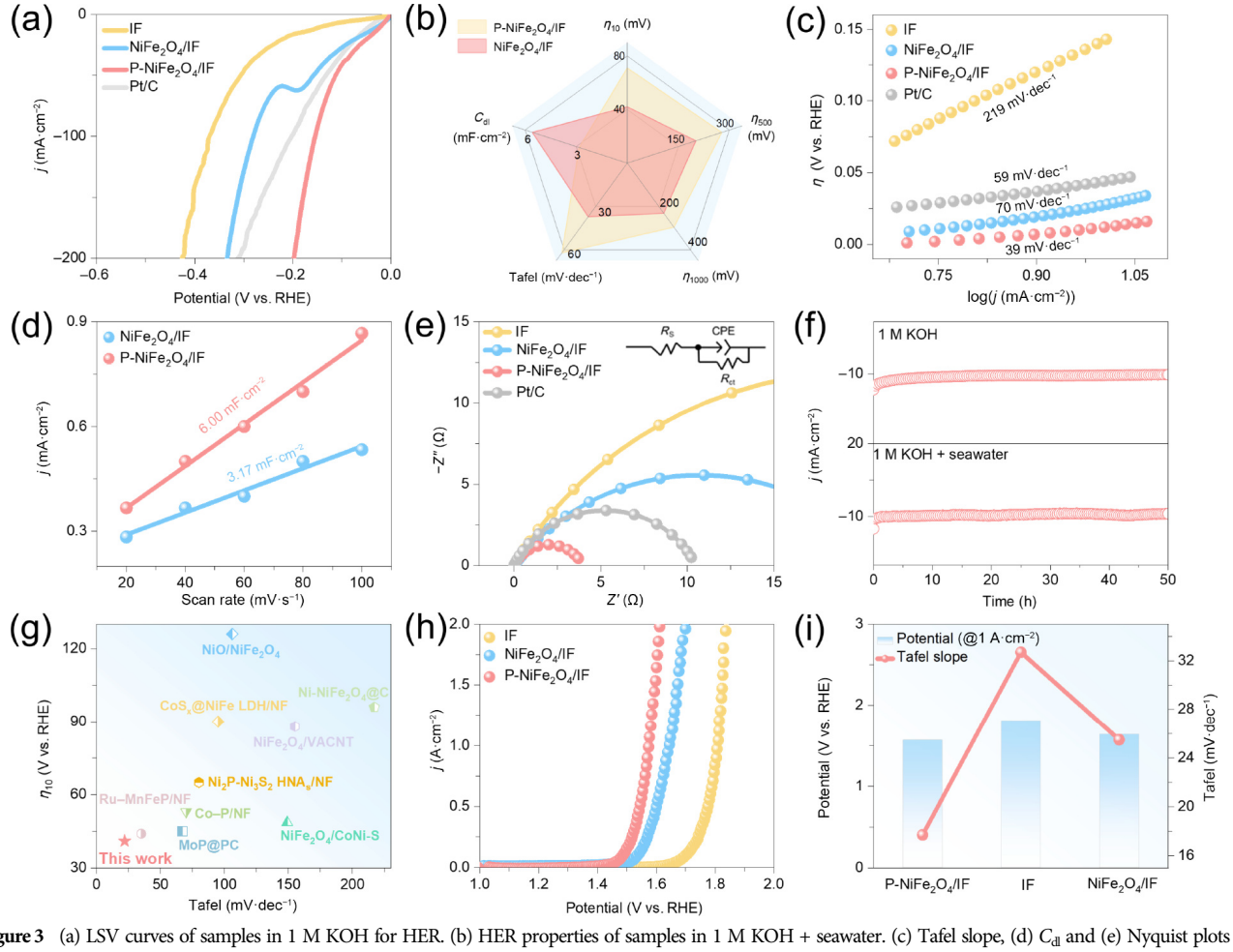


Figure 3 (a) LSV curves of samples in 1 M KOH for HER. (b) HER properties of samples in 1 M KOH + seawater. (c) Tafel slope, (d) C_{dl} and (e) Nyquist plots of samples in 1 M KOH. (f) The *i-t* testing of P-$NiFe_2O_4$/IF. (g) Comparison of P-$NiFe_2O_4$/IF in 1 M KOH with recently reported catalysts of HER performance. (h) OER LSV curves and (i) electrocatalytic properties of the prepared samples in 1 M KOH.

IF (η_{10} = 141 mV, η_{100} = 370 mV, and η_{500} = 475 mV). Furthermore, the η_{10} of P-$NiFe_2O_4$/IF exhibits 51.11% lower overpotential than the commercial Pt/C catalyst, underscoring its great application potential. The non-monotonic shape observed for the $NiFe_2O_4$/IF sample may originate from the reduction and reconstruction of the catalyst. Doping strategies are expected to suppress reductive reconstruction during the electrochemical process. To further evaluate practical applicability, the HER activity was also examined in 1 M KOH + seawater. In Fig. 3(b) and Fig. S3 in the ESM, P-$NiFe_2O_4$/IF displays markedly enhanced catalytic activity, requiring only 42 mV at 10 mA·cm^{-2} and 257 mV at 1 A·cm^{-2} in 1 M KOH + seawater, surpassing that of the reference samples and meeting the requirements for industrial-scale hydrogen production. Notably, P-$NiFe_2O_4$/IF maintains nearly unchanged performance in both simulated and real alkaline seawater compared with alkaline freshwater, demonstrating excellent corrosion resistance and seawater adaptability under harsh electrolysis conditions (Fig. S4 in the ESM) [36]. The HER kinetics of the catalysts were further investigated. As shown in Figs. 3(b) and 3(c) and Fig. S5 in the ESM, P-$NiFe_2O_4$/IF presents the minimum Tafel slopes of 39.0 mV·dec^{-1} (1 M KOH) and 38.5 mV·dec^{-1} (1 M KOH + seawater), suggesting rapid HER kinetics dominated by a Volmer-Heyrovsky mechanism [37]. From the cyclic voltammetry (CV) measurements, the double-layer capacitance (C_{dl}) values for P-$NiFe_2O_4$/IF are 6.00 mF·cm^{-2} (1 M KOH) and 5.78 mF·cm^{-2} (1 M KOH + seawater), surpassing those of the reference catalysts, indicating more exposed active sites and larger electrochemical active surface area (ECSA) (Figs. 3(b) and 3(d), Figs. S6–S8(a) in the ESM) [38]. More importantly, even after normalization, P-$NiFe_2O_4$/IF still demonstrates the optimal intrinsic activity in 1 M KOH and 1 M KOH + seawater, regardless of whether at low or high current densities (Figs. S8(b)–S8(d) in the ESM). These findings confirm that the superior catalytic performance of P-$NiFe_2O_4$/IF arises not only from its larger electrochemically active surface area but also from its intrinsically enhanced activity. Electrochemical impedance spectroscopy (EIS) measurements reveal markedly faster charge transfer, further supporting the enhanced HER kinetics of P-$NiFe_2O_4$/IF in 1 M KOH (Fig. 3(e)) [39]. Additionally, the P-$NiFe_2O_4$/IF catalyst exhibits excellent stability in both electrolytes, showing long-term stability for 50 h at 10 mA·cm^{-2} without obvious performance degradation (Fig. 3(f)). Notably, the lattice strain-engineered P-$NiFe_2O_4$/IF catalyst displays superior HER activity in different electrolytes, surpassing most previously reported HER catalysts (Fig. 3(g), Fig. S8(e) and Tables S1 and S2 in the ESM).

We further investigate the OER performance of the synthesized catalyst. In Figs. 3(h) and 3(i) and Fig. S9(a) in the ESM, P-$NiFe_2O_4$/IF achieves 1 A·cm^{-2} at merely 1.57 V (1 M KOH) and 1.55 V (1 M KOH + seawater), markedly lower than those of $NiFe_2O_4$/IF (1.64 V, 1.57 V) and IF (1.81 V, 1.78 V). To elucidate the OER reaction kinetics, we analyze the Tafel slopes of the catalysts. It (Fig. 3(i) and Figs. S9(b) and S9(c) in the ESM) indicates that P-$NiFe_2O_4$/IF exhibits lower Tafel slopes in both 1 M KOH (17.7 mV·dec^{-1}) and 1 M KOH + seawater (53.2 mV·dec^{-1}) compared with $NiFe_2O_4$/IF (25.5 and 76.1 mV·dec^{-1}), demonstrating that the strain generated by P doping effectively plays an important role in facilitating the oxygen evolution kinetics [37]. The introduction of strain also results in a notable reduction in charge transfer resistance, which accelerates the electron transfer process (Figs. S9(d) and S9(e) in the ESM) [39]. Additionally, the P-$NiFe_2O_4$/IF catalyst operates stably for 30 hours in both electrolyte environments (Fig. S10 in the ESM). Notably, P-$NiFe_2O_4$/IF exhibits superior OER performance compared with most reported catalysts in two alkaline systems (Fig. S11(a) and Table S3 in the ESM), demonstrating its practical application potential.

We have characterized the morphology and chemical valence state of P-$NiFe_2O_4$/IF after the HER/OER stability test. As shown in Figs. S11(b) and S11(c) in the ESM, SEM images indicate that P-$NiFe_2O_4$/IF retains its pre-reaction morphology after HER/OER. Post-HER valence state analysis indicates that all constituent elements remain present, with no significant change in their chemical states (Figs. S11(d)–S11(f) in the ESM. Figure S11(g) in the ESM confirms that Ni, Fe, O, and P elements are still detectable in the P-$NiFe_2O_4$/IF after the OER stability test. After the OER process, the Fe-P-related signal disappears, which can be attributed to surface reconstruction during the reaction (Fig. S11(h) in the ESM). Meanwhile, P may be oxidized into phosphate species and partially leached. In the P 2p spectrum, the characteristic peaks assigned to metal-phosphorus (M-P) coordination (Fig. S11(j) in the ESM, 129.4 and 130.3 eV) disappear, and the increased proportion of P-O species further supports this possible transformation. In addition, the positive shift in the Ni binding energy is observed after the stability test (Fig. S11(i) in the ESM), which may be attributed to the reconstruction of low-valence Ni into high-valence NiOOH phase during the OER process. This conclusion is further supported by *in situ* Raman results, where characteristic peaks appear at 481 and 561 cm^{-1}. It is widely accepted that high-valence Ni species serve as the key active sites for OER, significantly accelerating the reaction kinetics. Overall, the supplementary data provide solid confirmation of the long-term catalytic durability of P-$NiFe_2O_4$/IF.

3.3 Electrocatalytic mechanism investigation

3.3.1 *HER mechanism*

To reveal the key contributors to the improved catalytic performance, *in situ* Raman tests were applied for real-time tracking of the HER reaction dynamics in 1 M KOH. The broad O-H stretching band observed in the 3200–3800 cm^{-1} region (Fig. S12 in the ESM) is deconvoluted into three hydrogen-bonding states: tetra-hydrogen-bonded water (4HB-H_2O), di-hydrogen-bonded water (2HB-H_2O), and free water (Free-H_2O) [40]. It indicates that the 4HB-H_2O relative content on strained P-$NiFe_2O_4$/IF increases from 31.32% to 35.92% with increasing applied voltage, whereas only minor changes are observed for unstrained $NiFe_2O_4$/IF (Fig. 4(a)), indicating that strain effect favors to preserve the intact interfacial hydrogen-bond structure and facilitate proton transfer [41]. In addition, strain effect increases the electric-field dependence of interfacial water molecules, leading to more evident Stark shift. Specifically, 2HB-H_2O exhibits more pronounced Stark shift than 4HB-H_2O and free-H_2O for P-$NiFe_2O_4$/IF, indicating stronger modulation of its vibrational frequency by the local electric field (Fig. 4(b) and Fig. S12 in the ESM). This field effect weakens the O-H bond in 2HB-H_2O, leading to bond elongation and redshift of the O-H stretching mode, facilitating water dissociation and rendering 2HB-H_2O the dominant active water species in the HER [42]. Furthermore, hydrogen/deuterium (H/D) kinetic isotope effect (KIE) measurements reveal KIE value (> 1.5) for the P-$NiFe_2O_4$/IF catalyst, indicating rapid hydrogen transfer during the catalytic process (Fig. 4(c)) [43]. Overall, the strain effect induced by P doping facilitates proton transfer via the Grotthuss mechanism by

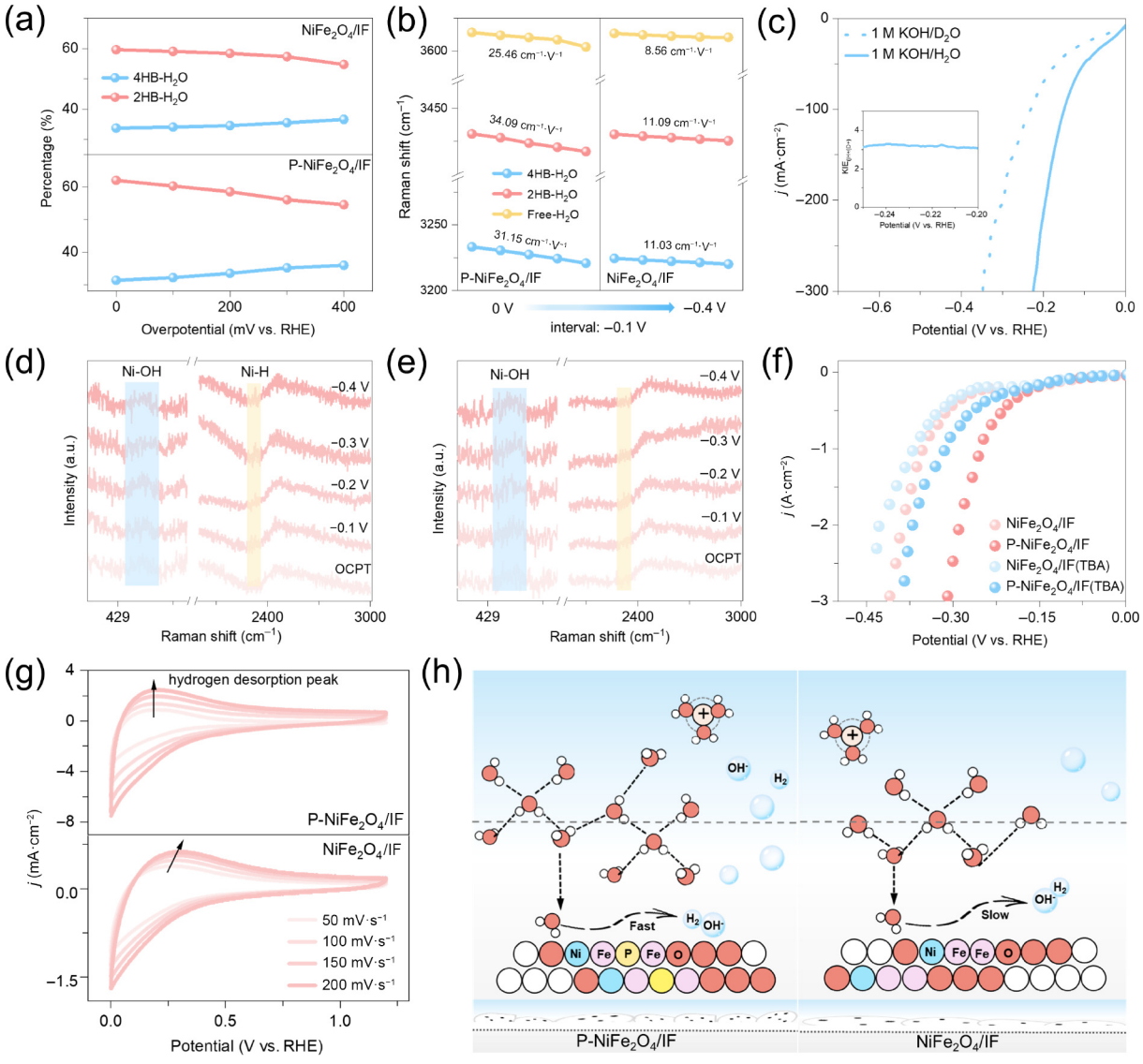


Figure 4 (a) Changes of interfacial water content during HER. (b) Shift in the OH-stretching vibrational frequency of interfacial water on P-$NiFe_2O_4$/IF and $NiFe_2O_4$/IF surfaces at varied HER overpotentials. (c) Polarization curves of P-$NiFe_2O_4$/IF in 1 M KOH/H_2O and 1 M KOH/D_2O solutions. *In situ* Raman spectra of (d) P-$NiFe_2O_4$/IF and (e) $NiFe_2O_4$/IF during HER process in 1 M KOH. (f) LSV curves of P-$NiFe_2O_4$/IF in 1 M KOH with/without TBA. (g) CV curves of P-$NiFe_2O_4$/IF under Ar protection. (h) Schematic mechanism for HER.

establishing continuous hydrogen bond network and accelerates water dissociation, enhancing HER kinetics. In the Raman spectra, apart from the water peak, the Ni-OH characteristic vibration peak at 513 cm^{-1} in P-$NiFe_2O_4$/IF exhibits significant attenuation at lower applied overpotentials (Figs. 4(d) and 4(e)) [44]. Thus, strain effect accelerates *OH desorption, reducing its surface coverage and alleviating competitive adsorption with *H to release active sites [42, 45]. Furthermore, the P-$NiFe_2O_4$/IF catalyst displays distinct vibrational peak at 2320 cm^{-1}, which can be unambiguously assigned to the stretching mode of the Ni-H bond [46]. The intensity of this peak remains high with increasing potential, indicating the persistent presence and substantial coverage of surface *H intermediates [47]. In contrast, this feature is absent in unstrained $NiFe_2O_4$/IF, suggesting that strain effect weakens excessive *OH adsorption, thereby facilitating stable *H accumulation as proton source to accelerate HER kinetics [48]. Peak assignment further confirms that Ni sites serve as the primary active centers for HER in P-$NiFe_2O_4$/IF [49]. Furthermore, the hydrogen desorption behavior constitutes core step in the HER. Tert-butyl alcohol (TBA) shows more pronounced activity decline for P-$NiFe_2O_4$/IF, indicating weaker hydrogen adsorption and thus preventing excessive *H accumulation (Fig. 4(f)) [50]. The desorption process was further evaluated using CV (Fig. 4(g)). Compared with $NiFe_2O_4$/IF, P-$NiFe_2O_4$/IF exhibits smaller shift and lower linear fitting slope (8×10^{-3} vs. 1.46×10^{-1}) in the hydrogen desorption peak potential with increasing scan rate, indicating faster hydrogen desorption kinetics (Fig. S13 in the ESM) [51, 52]. It can be concluded that strain effect maintains the continuity of the hydrogen bond network and accelerates water dissociation, significantly enhancing HER kinetics. Simultaneously, strain effect effectively alleviates OH-induced surface blockage, optimizes *H accumulation and desorption, and thereby enhances the activity of the HER (Fig. 4(h)).

3.3.2 *OER mechanism*

Structural evolution of the P-$NiFe_2O_4$/IF electrode was investigated via *in situ* Raman spectroscopy during OER (Fig. 5(a)).

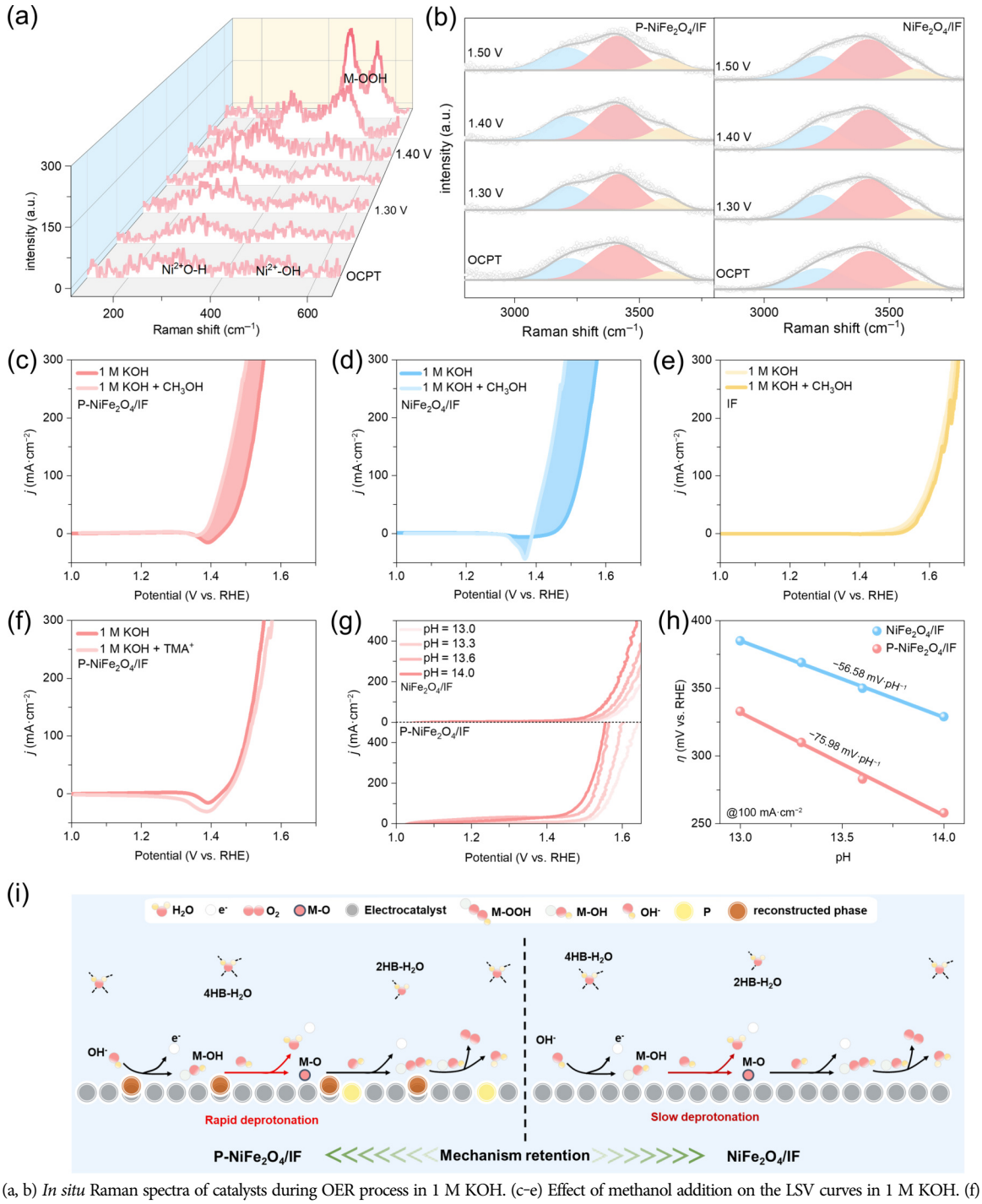


Figure 5 (a, b) *In situ* Raman spectra of catalysts during OER process in 1 M KOH. (c–e) Effect of methanol addition on the LSV curves in 1 M KOH. (f) Effect of TMA^+ addition on the LSV response of P-$NiFe_2O_4$/IF in 1 M KOH. (g) LSV curves of samples under different pH. (h) Potential-dependent pH profiles. (i) Schematic mechanism for OER.

The bands at 295 and 513 cm^{-1}, assigned to the E_g vibration of lattice $NiFe_2O_4$/IF and the A_{1g} stretching of Ni^{II}-OH from $Ni(OH)_2$, respectively [44, 53]. Above 1.45 V, these features disappear for the P-$NiFe_2O_4$/IF, replaced by the emergence of characteristic M-OOH (481 and 561 cm^{-1}, M = Ni) vibrations [54], whereas no analogous transformation is observed for the unstrained sample (Fig. S14 in the ESM). It indicates that lattice strain regulation promotes the formation of the catalytically active Ni-OOH phase, enabling catalytic activation at low overpotential [55]. Additionally, the interfacial water structure was analyzed by deconvoluting the O-H stretching region (3200–3800 cm^{-1}) to further investigate its correlation with catalytic behavior (Fig. 5(b)) [40]. As the applied potential increases, the 4HB-H_2O fraction on P-$NiFe_2O_4$/IF rises from 32.0% to 35.9% (Fig. S15 in the ESM), whereas only negligible change is observed on unstrained $NiFe_2O_4$/IF, suggesting the strain effect enhances the electric-field responsiveness of interfacial water and develops more continuous hydrogen-bond network to facilitate deprotonation [41]. The competitive methanol oxidation experiment was further employed to indirectly assess the extent of *OH species accumulation. By comparing the LSV curves collected with and without methanol, it is evident that lattice-strain regulation leads to more moderate *OH adsorption (Figs. 5(c)–5(e)) [56], which is expected to enhance hydrogen-bond network connectivity [13, 14]. The

marked reduction of *OH coverage observed for strained P-$NiFe_2O_4$/IF, relative to the unstrained sample, demonstrating the accelerated deprotonation process [57].

The tetramethylammonium cations (TMA^+) selectively bind $(O_2)^{n-}$ species and thereby inhibit lattice oxygen mechanism (LOM) activity [58]. As shown in Fig. 5(f) and Fig. S16 in the ESM, the OER activities of the catalysts with and without lattice strain regulation remain nearly unchanged upon the introduction of TMA^+ into the electrolyte, confirming that both catalysts follow the conventional AEM pathway [58]. The mechanism is further corroborated by the pH-dependent activity (Figs. 5(g) and 5(h)), demonstrating that $NiFe_2O_4$/IF exhibits weak pH dependence (–56.58 mV·pH^{-1}), verifying the occurrence of the AEM mechanism [59]. Notably, the P-$NiFe_2O_4$/IF electrocatalyst exhibits pronounced Nernstian shift (–75.98 mV·pH^{-1} vs. –59 mV·pH^{-1}), may resulting from the dynamic rearrangement of interfacial water molecules induced by strain effect [60]. Based on the above analysis, the lattice strain induced by P doping enhances the connectivity of the interfacial hydrogen-bond network, accelerating the deprotonation process. Meanwhile, the strain effect promotes active Ni-OOH formation and the transformation of key intermediates, collectively improving the OER reaction kinetics and catalytic performance (Fig. 5(i)).

3.4 DFT models and analysis

To uncover the source of the boosted electrocatalytic performance, density functional theory (DFT) calculations were conducted to evaluate the adsorption behavior of reaction intermediates. As illustrated in the Fig. 6(a) and Fig. S17 in the ESM, the constructed model was employed to represent the realistic surface structure of the catalyst. The calculated hydrogen adsorption free energy (ΔG_{*H}, Fig. 6(b)) shows that P-$NiFe_2O_4$ exhibits a ΔG_{*H} value of –0.27 eV, which is much closer to thermoneutrality than unstrained $NiFe_2O_4$ (0.43 eV), indicating optimized *H adsorption strength and subsequent H_2 desorption [61]. In addition, site-dependent calculations reveal that the Ni site possesses more favorable ΔG_{*H} (–0.27 eV) than the Fe and O sites (0.32 eV and –1.09 eV), suggesting that Ni acts as the dominant active site for HER [62], in agreement with the experimental results (Fig. 6(c) and Fig. S18 in the ESM). As the key intermediate in both reactions, the adsorption behavior of *OH directly determines the HER and OER reaction process. According to theoretical calculations, P-$NiFe_2O_4$ exhibits weaker *OH adsorption than $NiFe_2O_4$ (Fig. 6(d)), thereby avoiding the high-barrier *OH deprotonation step and the occupation of active sites, creating more favorable reaction conditions for both HER and OER processes [63, 64]. The optimized regulation of intermediate adsorption behavior, combined with the benefits of the continuous hydrogen-bond network, guarantees the outstanding catalytic activity (Fig. 6(e)).

3.5 Overall water splitting

Given the P-$NiFe_2O_4$/IF excellent performances in both HER and OER, we further explored its industrial application potential. When employed as both electrodes in a two-electrode electrolyzer, P-$NiFe_2O_4$/IF achieves remarkable overall water splitting activity, delivering 10 mA·cm^{-2} and 1 A·cm^{-2} at cell voltages of 1.54 V and 1.86 V, outperforming the commercial Pt/C||RuO_2 system (Figs. 7(a) and 7(b)). Multi-step chronoamperometry reveals rapid response of the P-$NiFe_2O_4$/IF||P-$NiFe_2O_4$/IF electrolyzer with sustained stability upon potential variations (Fig. 7(c)). Additionally, 150-hour constant current durability test of the P-$NiFe_2O_4$/IF||P-$NiFe_2O_4$/IF electrolyzer shows negligible current decay, confirming its outstanding electrochemical stability during prolonged operation (Fig. 7(d)). To assess the charge utilization efficiency during the catalytic process, the Faradaic efficiency of the two-electrode system was measured using a single-chamber H-type electrolyzer (Fig. S19 in the ESM). The system achieves Faradaic efficiency exceeding 97%, with the H_2:O_2 volume ratio stably maintained at 2:1 over the entire electrolysis period (Fig. 7(e) and Fig. S20 in the ESM). Furthermore, the P-$NiFe_2O_4$/IF||P-$NiFe_2O_4$/IF electrolyzer can sustain continuous hydrogen production by harnessing common energy sources including batteries and solar energy, validating the effectiveness and feasibility of this system for hydrogen generation (Fig. S21 in the ESM).

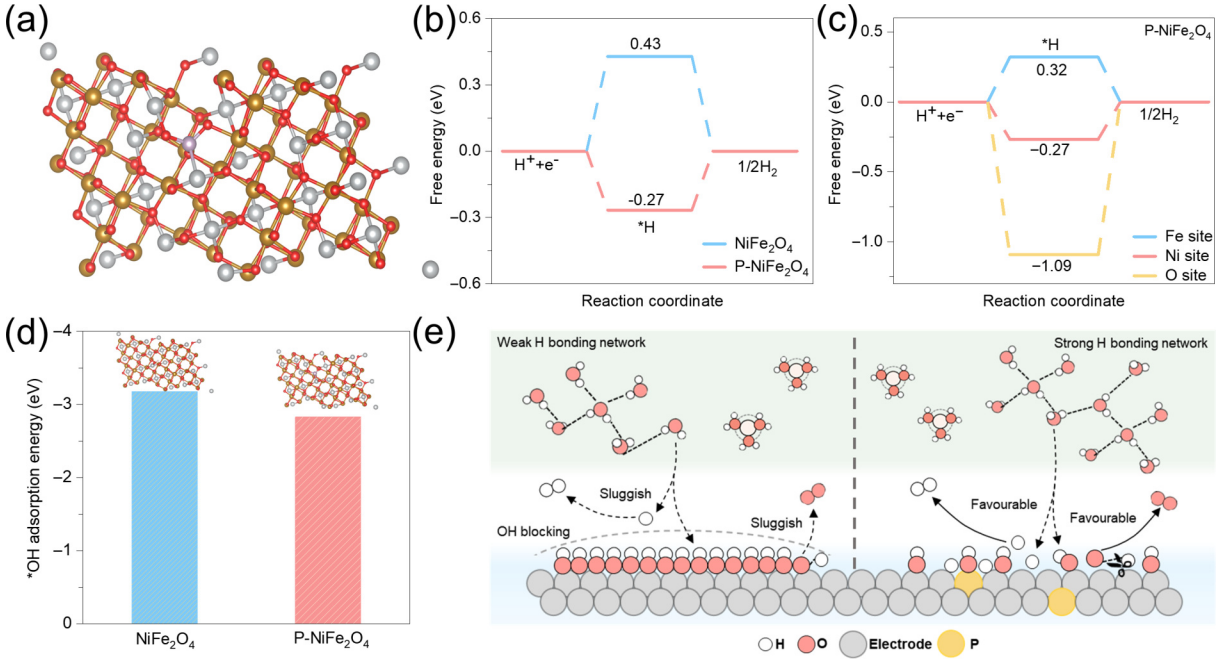


Figure 6 (a) The structural model of P-$NiFe_2O_4$/IF. (red: O, grey: Ni, brown: Fe). The purple spheres represent P atoms. (b) ΔG_{*H} for $NiFe_2O_4$/IF and P-$NiFe_2O_4$/IF. (c) ΔG_{*H} at different sites of P-$NiFe_2O_4$/IF. (d) *OH adsorption energy (the inset shows the *OH adsorption models). (e) Mechanism schematic.

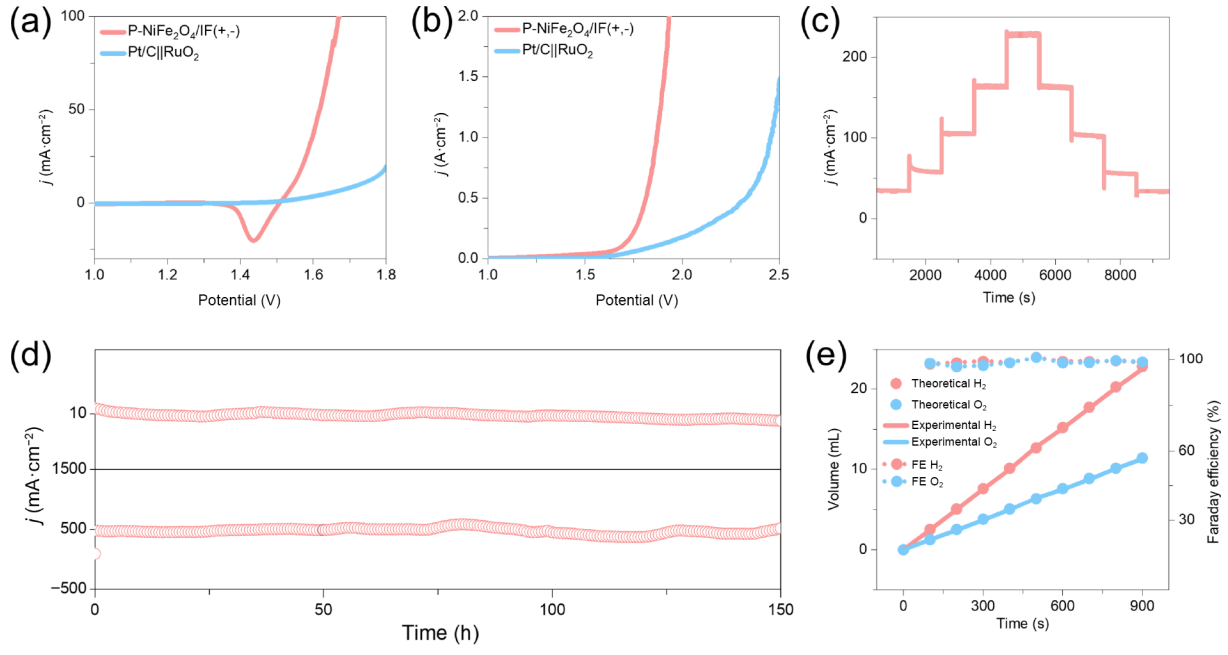


Figure 7 (a, b) LSV curves of P-$NiFe_2O_4$/IF||P-$NiFe_2O_4$/IF and Pt/C||RuO_2 for overall water splitting. (c) Multi-step chronoamperometry curve. (d) The *i-t* curves of P-$NiFe_2O_4$/IF||P-$NiFe_2O_4$/IF. (e) The Faraday efficiency of P-$NiFe_2O_4$/IF.

4 Conclusion

In summary, this study successfully realizes the *in-situ* growth of P-$NiFe_2O_4$/IF catalysts on IF via corrosion-annealing coupled strategy. The developed synthesis approach not only preserves the intrinsic porous architecture of the IF substrate but also endows the catalyst with seaurchin-like morphology and superior hydrophilicity, accelerating mass transfer and enhancing the exposure of active sites. Moreover, *in situ* Raman reveals that strain effect strengthens the hydrogen-bond interactions between the catalyst and interfacial water, leading to more continuous hydrogen-bond network. DFT calculations further show that P-$NiFe_2O_4$/IF exhibits more favorable adsorption strengths of *H and *OH intermediates compared with $NiFe_2O_4$/IF, avoiding *OH poisoning and hindered dissociation, synergistically optimizing both HER and OER processes. Benefiting from these synergistic features, the P-$NiFe_2O_4$/IF||P-$NiFe_2O_4$/IF electrolyzer achieves low operating voltage and remarkable durability, underscoring its potential for high-efficiency, sustainable hydrogen generation. This study provides meaningful guidance for the rational design of efficient electrocatalysts.

Acknowledgements

The authors thank funding support from the National Natural Science Foundation of China (52371227 and 22278175), Taishan Scholar Young Talent Program (tsqn202408200), Shandong Province "Double-Hundred Talent Plan" (WST2020003), Zhejiang Provincial Natural Science Foundation of China (Grant No. LZ24B060001), State Key Laboratory of New Textile Materials and Advanced Processing, Wuhan Textile University (FZ 2025022).

Electronic Supplementary Material: Supplementary material (experimental details; materials characterizations; electrochemical characterizations and addition details about DFT calculations) is available in the online version of this article at https://doi.org/10.26599/NRE.2026.9120238.

References

[1] Huo, M. T.; Liang, Y.; Qin, K. C.; Wang, G. Z.; Xing, Z. H.; Chang, J. F. Hexavalent iridium boosts oxygen evolution performance. *Green Carbon* **2024**, *2*, 403–404.

[2] Zou, R. Q.; Liu, S. B.; Su, J.; Ding, W. H.; Wang, Y. J.; Yan, F.; Guo, P.; Zhou, J. C.; Zhang, Y. Z.; Li, X. H. Nickel carrier transfer bridge for improved photocatalytic water splitting of Zn_2GeO_4. *Trans. Mater. Res.* **2025**, *1*, 100006.

[3] Liu, G. B.; Xu, Y. S.; Yang, T.; Jiang, L. H. Recent advances in electrocatalysts for seawater splitting. *Nano Mater. Sci.* **2023**, *5*, 101–116.

[4] Zhou, X. Y.; Yang, T. T.; Li, T.; Zi, Y. J.; Zhang, S. J.; Yang, L.; Liu, Y. K.; Yang, J.; Tang, J. J. *In-situ* fabrication of carbon compound NiFeMo-P anchored on nickel foam as bi-functional catalyst for boosting overall water splitting. *Nano Res. Energy* **2023**, *2*, e9120086.

[5] Lin, Y. X.; Liang, B. M.; Hu, Y. G.; Zhao, K. K.; Wang, Z. K.; Zheng, K.; Xi, H. X.; Duan, C. X.; Sun, X. J. Recent advances in catalysts toward alkaline oxygen evolution reaction (OER). *Environ. Chem. Saf.* **2025**, *1*, 9600012.

[6] Shi, Y.; Song, L. M.; Liu, Y.; Wang, T. T.; Li, C. X.; Lai, J. P.; Wang, L. Dual cocatalytic sites synergize NiFe layered double hydroxide to boost oxygen evolution reaction in anion exchange membrane water electrolyzer. *Adv. Energy Mater.* **2024**, *14*, 2402046.

[7] Zhou, Y. S.; Wang, Z. T.; Cui, M. H.; Wu, H. Y.; Liu, Y. J.; Ou, Q. R.; Tian, X. L.; Zhang, S. Y. NiFe‐based electrocatalysts for alkaline oxygen evolution: Challenges, strategies, and advances toward industrial‐scale deployment. *Adv. Funct. Mater.* **2024**, *34*, 2410618.

[8] Huang, J. Z.; Wang, R.; Sheng, H. Y.; Zhu, X. R.; Dominic Ross, R.; Hua, D. X.; Lin, L.; Li, Y. F.; Zhang, Q. H.; Gu, L. et al. Isotope-dependent Tafel analysis probes proton transfer kinetics during electrocatalytic water splitting. *Nat. Chem.* **2026**, *18*, 669–676.

[9] Li, J. Z.; Cheng, H. Y.; Sun, Y. N.; Ma, R. Z.; Li, D. N.; Xu, Y. C.; Jin, J. H.; Liu, X.; Shao, M. F.; Wang, L. Scalable ruthenium core-shell hydrogen catalyst for efficient and robust proton-exchange membrane electrolyser. *Nat. Mater.* **2026**, *25*, 238–248.

[10] Gu, M. Z.; Jiang, L.; Wang, H.; Chen, Q.; Hao, Y. X.; Li, L. L.; Hu, F.; Zhang, X. J.; Wu, Y. P.; Wang, G. F. et al. Iodine-induced

redirection of active sources in Cu-based catalysts during efficient and stable water oxidation. *J. Am. Chem. Soc.* **2025**, *147*, 19675–19686.
[11] Hassanali, A.; Giberti, F.; Cuny, J.; Kühne, T. D.; Parrinello, M. Proton transfer through the water gossamer. *Proc. Natl. Acad. Sci. USA* **2013**, *110*, 13723–13728.
[12] Shi, G. S.; Lu, T. Y.; Zhang, L. M. Understanding the interfacial water structure in electrocatalysis. *Natl. Sci. Rev.* **2024**, *11*, nwae241.
[13] Lin, Y. R.; Xie, S. H.; Chen, K.; Chen, J. X.; Kang, B. Y.; Wang, H. B.; Lu, Z. W.; Huang, J. H.; Wen, Z. H. Bridging acidic and alkaline hydrogen electrocatalysis via Ru-modified Pt_3Co for waste-to-energy electrochemical neutralization fuel cells. *Adv. Mater.* **2026**, *38*, e20173.
[14] Zuo, S. Y.; Wang, Y.; Wan, J. Q.; Yi, J. X. Hydrogen bonding network in the electrical double layer mediates fast proton skipping to get rid of Fenton reaction pH dependence enables highly efficient alkaline water purification. *Water Res.* **2025**, *268*, 122612.
[15] Wang, S.; Zhang, J. C.; Jia, S. Y.; Liu, Q. C.; Li, J. L.; Wang, J. L.; Tang, Y. W.; Sun, H. J. Alleviating OH blockage: Asymmetric adsorption configuration of Co-OH-M (d^{10}) for seawater electrolysis. *ACS Catal.* **2026**, *16*, 3851–3863.
[16] Dickens, C. F.; Nørskov, J. K. A theoretical investigation into the role of surface defects for oxygen evolution on RuO_2. *J. Phys. Chem. C* **2017**, *121*, 18516–18524.
[17] Liang, X. H.; Zhang, Z. H.; Wang, Z.; Hu, M. Z.; Cheng, D.; Jiang, Y.; Ren, H.; Shen, F. Y.; Yang, S. T.; Yang, X. X. et al. Breaking the H_2O dissociation-OH desorption scaling relationship in alkaline hydrogen evolution by oxophilic single atom M_1-Ru_n electrocatalysts. *Energy Environ. Sci.* **2025**, *18*, 4302–4311.
[18] Mushtaq, M.; Zhu, Z. X.; Yang, H.; Khanam, Z.; Hu, Y. W.; Mathi, S.; Wang, Z. M.; Balogun, M. S.; Huang, Y. C. Lattice strain-modulated trifunctional $CoMoO_4$ polymorph-based electrodes for asymmetric supercapacitors and self-powered water splitting. *Small* **2025**, *21*, 2409418.
[19] Liu, J.; Xu, F.; Cen, M. S.; Tang, D. S.; Wu, L. Q.; Pang, Y. F.; Huang, Y. C.; Chen, J.; Yang, H.; Hu, Y. W. Lattice stress memory in CoNiP@Cu_3P core-shell nanoarchitectures enabling self-adaptive ultra-efficient hydrogen evolution. *J. Catal.* **2026**, *454*, 116591.
[20] Zhang, T.; Song, W. Q.; Wang, X.; Qiao, P. Z.; Feng, J. H.; Shi, H. C.; Wang, H. Z.; Yang, X. Y.; Zhang, J. F.; Ding, J. et al. Lattice coupling enables gradient strain tuning toward platinum skin at intermetallic nanocatalysts for boosting hydrogen electrocatalysis. *Adv. Mater.* **2026**, *38*, e11865.
[21] Li, X.; Hou, S. S.; Xie, X. X.; Yang, H.; Huang, Y. C. Lattice strain engineering via electrochemical treatment boosts solar water oxidation of $BiVO_4$ through accelerated intermediate conversion. *J. Catal.* **2026**, *453*, 116540.
[22] Chen, Z. J.; Han, N.; Wei, W.; Chu, D. W.; Ni, B. J. Dual doping: An emerging strategy to construct efficient metal catalysts for water electrolysis. *EcoEnergy* **2024**, *2*, 114–140.
[23] Zhao, H. X.; Jiang, X.; Jin, M. J.; Song, J. Q.; Li, M. X.; Zhou, J. Y.; Pan, X. J. Construction of urchin-like bimetallic phosphides induced by carbon dots for efficient wide pH hydrogen production. *J. Colloid Interface Sci.* **2023**, *652*, 1208–1216.
[24] Sun, Y. K.; Dai, J. J.; Lv, H.; Dong, L.; Wang, Z. Y.; Feng, H.; Meng, B. X.; Li, Z. J. Superhydrophilic V-doped CoP nanoparticles@Cu_3P nanotubes with vacancy and interface engineering for synergistically enhanced electrocatalytic overall water splitting. *Adv. Funct. Mater.* **2025**, *35*, 2505867.
[25] Tang, Z.; Dong, Z. L.; Yuan, L. J.; Li, B. W.; Zhu, Y. L. Unlocking the potential: Key roles of interfacial water in electrocatalysis. *EES Catal.* **2025**, *3*, 943–971.
[26] Peng, Y.; Huang, C. R.; Huang, J. L.; Feng, M.; Qiu, X. Z.; Yue, X.; Huang, S. M. Filling octahedral interstices by building geometrical defects to construct active sites for boosting the oxygen evolution reaction on $NiFe_2O_4$. *Adv. Funct. Mater.* **2022**, *32*, 2201011.
[27] Chen, J. L.; Jiang, M. M.; Zhang, F. Z.; Wang, L.; Yang, J. P. Interstitial boron atoms in Pd aerogel selectively switch the pathway for glycolic acid synthesis from waste plastics. *Adv. Mater.* **2024**, *36*, 2401867.
[28] Liu, C. H.; Chen, X. X.; Zhang, X. X.; Li, J.; Wang, B. W.; Luo, Z. Y.; Li, J. H.; Qian, D.; Liu, J. L.; Waterhouse, G. I. N. Sodium tartrate-assisted synthesis of high-purity $NiFe_2O_4$ nano-microrods supported by porous ketjenblack carbon for efficient alkaline oxygen evolution. *J. Phys. Chem. Lett.* **2023**, *14*, 6099–6109.
[29] Liu, S. L.; Wang, Y.; Zhao, H. L.; Li, H. D,; Xiao, W. P.; Xiao, Z. Y.; Xu, G. R.; Chen, D. H.; Wu, Z. X.; Wang, L. Amorphous W-doped iron phosphide with superhydrophilic surface to boost water-splitting under large current density. *Chem. Eng. J.* **2024**, *496*, 153956.
[30] Li, X. J.; Wu, T. T.; Li, N.; Zhang, S. T.; Chang, W. J.; Chi, J. Q.; Liu, X. B.; Wang, L. Vertically staggered porous Ni_2P/Fe_2P nanosheets with trace Ru doping as bifunctional electrocatalyst for alkaline seawater splitting. *Adv. Funct. Mater.* **2024**, *34*, 2400734.
[31] Guo, H.; Zhu, S. S.; Zhang, Z. H.; Pan, L.; Jiang, H. M.; Siddiqui, N. A.; Khan, A.; Lin, J. J. Oxygen vacancies and phosphorus-doped P-WO_{3-x}/CC electrocatalysts boosting hydrogen evolution reaction. *Chem. -Eur. J.* **2025**, *31*, e202501239.
[32] Deng, T.; Jia, S. Q.; Xue, C.; Cheng, H. L.; Jiao, J. P.; Chen, X.; Xia, Z. H.; Dong, M. K.; Chen, C. J.; Wu, H. H. et al. Phosphorus-doped Cu/Fe_2O_3 electrocatalysts with optimized synergy between the different sites for efficient urea electrosynthesis. *J. Am. Chem. Soc.* **2025**, *147*, 32924–32931.
[33] Du, Y.; Li, H.; Yin, Y. H.; Sun, D. N.; Li, N.; Wang, B. D. *Operando* tracking of hydrazine intermediate reveals the Gerischer-Marcus pathway for ammonia electrooxidation on oxygen-deficient CuO. *Angew. Chem., Int. Ed.* **2026**, *65*, e24377.
[34] Liu, S. J.; Wu, G. Z.; Jiang, J. D.; Yang, Y. D.; Du, A. J.; Zhang, W. Y.; Mao, X.; Dai, L.; Qin, Q. Electrochemical lattice engineering of bismuthene for selective glycine synthesis. *Adv. Mater.* **2025**, *37*, 2500843.
[35] Sun, M. T.; Zhou, W.; Huang, Y. M.; Yu, Y.; Zhang, X. W.; Chen, J. X.; Yuan, J. S.; Li, W. J.; Feng, Y. L.; Chen, S. et al. Mn enhanced dynamic catalysis on NiCoMnS/NF in urea electrooxidation: Insights into Mn^{2+}/Mn^{4+} redox cycle. *Adv. Funct. Mater.* **2026**, *36*, e11986.
[36] Song, L. M.; Zhang, D.; Miao, H. F.; Shi, Y.; Wang, M. N.; Zhao, L.; Zhan, T. R.; Lai, J. P.; Wang, L. Interstitial atom-doped NiFe alloy as pre-catalysts boost direct seawater oxygen evolution. *Appl. Catal. B: Environ.* **2024**, *342*, 123376.
[37] Guo, Y. J.; Guo, D.; Ye, F.; Wang, K.; Shi, Z. Q.; Chen, X. J.; Zhao, C. Self-supported $NiSe_2$ nanowire arrays on carbon fiber paper as efficient and stable electrode for hydrogen evolution reaction. *ACS Sustain. Chem. Eng.* **2018**, *6*, 11884–11891.
[38] Wang, P.; Zheng, J.; Li, Y. Y.; Shi, Q. F.; Zhang, J.; Wan, Y.; Niu, M.; Yamauchi, Y.; Long, Y. Z. Catalyst for industrial-scale seawater electrolysis: Inhibit active metal dissolution and chlorine corrosion. *Adv. Sci.* **2025**, *12*, e14301.
[39] Wang, M. Y.; Zhao, Y. J.; Miao, H.; Wei, Z. High crystallinity of self-assembled iron phthalocyanine enhanced photocatalytic properties for wastewater treatment. *Environ. Chem. Saf.* **2025**, *1*, 9600040.
[40] Zhao, Y.; Li, Q. Q.; He, Q. F.; Ren, P. W.; Zhang, D. A.; Wang, Y. H.; Dong, J. C.; Zheng, S. S.; Zhang, Y. J.; Yang, Z. L. et al. *In situ* Raman spectroscopy reveals the multifunctional role of interfacial water in CO_2-to-C_2 electroreduction on Cu(*hkl*) surfaces. *J. Am. Chem. Soc.* **2025**, *147*, 30230–30238.
[41] Yang, C. Y.; Yue, J. C.; Wang, G. Q.; Luo, W. Activating and identifying the active site of RuS_2 for alkaline hydrogen oxidation electrocatalysis. *Angew. Chem., Int. Ed.* **2024**, *63*, e202401453.
[42] Zhang, C. Y.; Yang, G.; Gao, X. Q.; Li, Z. Y.; Li, Y. F.; Wang, S. Y.; Wang, J. Y.; Zhao, X. H.; Zhang, K.; Kang, Y. et al. Tuning Lewis basicity of surface OH species on nickel (hydro)oxides towards efficient hydrogen evolution. *Appl. Catal. B: Environ. Energy* **2025**, *377*, 125478.
[43] Guan, X. Y.; Wu, Q. N.; Li, H. B.; Zeng, S. Y.; Yao, Q. X.; Li, R.; Chen, H. Y.; Zheng, Y.; Qu, K. G. Identifying the roles of Ru single

atoms and nanoclusters for energy-efficient hydrogen production assisted by electrocatalytic hydrazine oxidation. *Appl. Catal. B: Environ.* **2023**, *323*, 122145.

[44] Plonska-Brzezinska, M. E.; Brus, D. M.; Molina-Ontoria, A.; Echegoyen, L. Synthesis of carbon nano-onion and nickel hydroxide/oxide composites as supercapacitor electrodes. *RSC Adv.* **2013**, *3*, 25891–25901.

[45] Zhang, Y. J.; Li, Z. J.; Jang, H.; Kim, M. G.; Cho, J.; Liu, S. G.; Liu, X. E.; Qin, Q. *In situ* grown RuNi alloy on $ZrNiN_x$ as a bifunctional electrocatalyst boosts industrial water splitting. *Adv. Mater.* **2025**, *37*, 2501586.

[46] Qiu, L. Y.; Tian, F. Y.; He, L.; Li, M. G.; Lin, F. X.; Li, L.; Ren, X.; Wu, F. Y.; Li, L. L.; Zhang, T. B. et al. Robust interfacial hydrogen-bond network on positively charged Ru-N-Ni dual sites boosts alkaline hydrogen electrocatalysis. *Adv. Mater.* **2026**, *38*, e12568.

[47] Chen, J. D.; Chen, C. H.; Qin, M. K.; Li, B.; Lin, B. B.; Mao, Q.; Yang, H. B.; Liu, B.; Wang, Y. Reversible hydrogen spillover in Ru-WO_{3-x} enhances hydrogen evolution activity in neutral pH water splitting. *Nat. Commun.* **2022**, *13*, 5382.

[48] Zhou, L. L.; Wan, T.; Zhong, Y.; Liu, W.; Yu, L. F.; Li, T. S.; Sun, K.; Waterhouse, G. I. N.; Xu, H. J.; Kuang, Y. et al. Ampere-level hydrogen generation via 1000 H stable seawater electrolysis catalyzed by Pt-cluster-loaded NiFeCo phosphide. *Small* **2024**, *20*, 2406076.

[49] Shen, S. J.; Li, Q. G.; Zhang, H. H.; Yang, D.; Gong, J. J.; Gu, L.; Gao, T.; Zhong, W. W. Negative-valent platinum stabilized by Pt-Ni electron bridges on oxygen-deficient NiFe-LDH for enhanced electrocatalytic hydrogen evolution. *Adv. Mater.* **2025**, *37*, 2500595.

[50] Zhang, Y.; Ma, C. Q.; Zhu, X. J.; Qu, K. Y.; Shi, P. D.; Song, L. Y.; Wang, J.; Lu, Q. P.; Wang, A. L. Hetero-interface manipulation in MoO_x@Ru to evoke industrial hydrogen production performance with current density of 4000 $mA \cdot cm^{-2}$. *Adv. Energy Mater.* **2023**, *13*, 2301492.

[51] Li, Y. F.; Li, L. S.; Xu, S. L.; Cui, K.; Wang, T. S.; Jiang, Z.; Li, J. Y. Hydrogen spillover mechanism at the metal-metal interface in electrocatalytic hydrogenation. *Angew. Chem., Int. Ed.* **2024**, *63*, e202407810.

[52] Dai, J.; Zhu, Y. L.; Chen, Y.; Wen, X.; Long, M. C.; Wu, X. H.; Hu, Z. W.; Guan, D. Q.; Wang, X. X.; Zhou, C. et al. Hydrogen spillover in complex oxide multifunctional sites improves acidic hydrogen evolution electrocatalysis. *Nat. Commun.* **2022**, *13*, 1189.

[53] Xu, W. J.; Dang, J. Y.; Zhang, X. Y.; Xie, D.; Zhang, J. P. Hole-doping driven electronic structure reconstruction enables dual-site synergistic regulation and energy barrier balancing in $NiFe_2O_4$ for efficient seawater oxygen evolution. *Adv. Funct. Mater.* **2026**, *36*, e21621.

[54] Wang, X. J.; Zhao, H. L.; Li, H. D.; Xiao, W. P.; Xu, G. R.; Fu, G. Y.; Wang, L.; Wu, Z. X. Long-range disordered MoZn electrocatalyst with a synergistic AEM-LOM mechanism for efficient oxygen evolution. *Inorg. Chem. Front.* **2025**, *12*, 8118–8127.

[55] Zhao, H. L.; Tian, F. Y.; Xiao, W. P.; Xu, G. R.; Zhang, X. Y.; Wang, L.; Wu, Z. X. Microwave-synthesized PtFe alloy nanosheets on nickel foam for efficient overall water splitting via synergistic HER/OER optimization mechanism. *Chem. Eng. J.* **2025**, *522*, 167641.

[56] Chen, X.; Xu, X. Y.; Cheng, Y. W.; Liu, H.; Li, D. D.; Da, Y. M.; Li, Y. T.; Liu, D. M.; Chen, W. Achieving high-performance electrocatalytic water oxidation on $Ni(OH)_2$ with optimized intermediate binding energy enabled by S-doping and CeO_2-Interfacing. *Small* **2024**, *20*, 2303169.

[57] Chen, Y. H.; Guo, C. B.; Wang, Y.; Wang, K.; Song, S. Q. Constructing high-entropy spinel oxide thin films via magnetron sputtering for efficiently electrocatalyzing alkaline oxygen evolution reaction. *Chin. J. Catal.* **2025**, *77*, 210–219.

[58] Li, X.; Deng, C.; Kong, Y.; Huo, Q. H.; Mi, L. R.; Sun, J. J.; Cao, J. Y.; Shao, J. X.; Chen, X. B.; Zhou, W. L. et al. Unlocking the transition of electrochemical water oxidation mechanism induced by heteroatom doping. *Angew. Chem., Int. Ed.* **2023**, *62*, e202309732.

[59] Jia, W. Q.; Cao, X. J.; Chen, X. J.; Qin, H. Y.; Miao, L. C.; Wang, Q. L.; Jiao, L. F. γ-MnO_2 as an electron reservoir for RuO_2 oxygen evolution catalyst in acidic media. *Small* **2024**, *20*, 2310464.

[60] Huang, J. Z.; Clark, A. H.; Hales, N.; Crossley, K.; Guehl, J.; Skoupy, R.; Schmidt, T. J.; Fabbri, E. Oxidation of interfacial cobalt controls the pH dependence of the oxygen evolution reaction. *Nat. Chem.* **2025**, *17*, 856–864.

[61] Jiang, J. H.; Xu, G. C.; Gong, B. B.; Zhu, J. J.; Wang, W. W.; Zhao, T.; Feng, Y. Y.; Wu, Q. H.; Liu, S.; Zhang, L. Hydrogen spillover mechanism of superaerophobic $NiSe_2$-Ni_5P_4 electrocatalyst to promote hydrogen evolution in saline water. *Adv. Funct. Mater.* **2025**, *35*, 2412685.

[62] Hou, L. Q.; Li, Z. J.; Jang, H.; Kim, M. G.; Cho, J.; Zhong, W. W.; Liu, S. G.; Liu, X. E. Partially interstitial silicon-implanted ruthenium as an efficient electrocatalyst for alkaline hydrogen evolution. *Angew. Chem., Int. Ed.* **2025**, *64*, e202423756.

[63] Yao, H. X.; Fan, Z.; Xu, L. L.; Wang, X. K.; Chu, L.; Kong, Z. H.; Zhang, C. H.; Zhou, J.; Zheng, L. R.; Huang, M. H. et al. Triadic site-mediated hydroxyl/hydrogen dual spillover effect to boost alkaline hydrogen evolution reaction. *Adv. Energy Mater.* **2025**, *15*, e04124.

[64] Zhang, D.; Liu, H.; Liu, J.; Shi, Y.; Song, B.; Chen, Y. Y.; Li, C. Y.; Li, S. D.; Kang, M. Z.; Zhang, H. F. et al. B-doping tuning oxygen vacancies facilitates mechanism transition in RuO_2 for oxygen evolution at high current density. *Adv. Funct. Mater.* **2026**, *36*, e29621.



Xiaojun Wang is currently pursuing her master's degree at the College of Chemistry and Molecular Engineering, Qingdao University of Science and Technology, under the supervision of Professor Zexing Wu. Her research focuses on designing non-carbon supported electrocatalysts via corrosion engineering, for water/seawater splitting.



Prof. Lei Li is a professor at the College of Biological, Chemical Sciences and Engineering, Jiaxing University. He obtained his Ph.D. from Fuzhou University in 2009 and was promoted to Professor in 2018. His research focuses on green catalytic materials and low-carbon chemical engineering, especially hydrogen production and conversion of carbon dioxide. He has published more than 50 papers as first/corresponding author in journals including *Nature Communications*, *ACS Nano* and *Advanced Functional Materials*. He has been selected as a leading high-level top-notch talent in Zhejiang provincial universities. He was awarded the second prize of the Science and Technology Progress Award of China Nonferrous Metals Industry.



Prof. Lei Wang was awarded a Ph.D. in chemistry from Jilin University in 2006 under the supervision of Prof. Shouhua Feng. He moved to Shandong University, The State Key Laboratory of Crystal Materials, as a Postdoctoral Scholar from 2008 to 2010. He is currently a professor of chemistry at Qingdao University of Science and Technology. His research interests mainly focus on the design and synthesis of functional organic-inorganic hybrids and porous MOFs materials, as well as their applications in photocatalysis, electrocatalysis, lithium-ion battery, etc.



Prof. Zexing Wu is currently a professor of School of College of Chemistry and Molecular Engineering at Qingdao University of Science and Technology. He earned his Ph.D. (2017) from Huazhong University of Science and Technology. His research interests focus on designing non-carbon supported electrocatalysts, through microwave quasi-solid and corrosion engineering, for water splitting.